

Article

A Multichannel Superconductor-Based Photonic Crystal Optical Filter Tunable in the Visible and Telecom Windows at Cryogenic Temperature

Luz E. González ^{1,2,*} , Lina M. Segura-Gutierrez ³, John E. Ordoñez ^{3,4} , Gustavo Zambrano ^{3,4} 
and John H. Reina ^{2,5} 

¹ Facultad de Ciencias Naturales y Matemáticas, Universidad de Ibagué, Ibagué 730001, Colombia

² Centre for Bioinformatics and Photonics (CIBioFi), Universidad del Valle, Edificio E20 No. 1069, Cali 760032, Colombia; john.reina@correounivalle.edu.co

³ Thin Films Group, Departamento de Física, Universidad del Valle, Cali 760032, Colombia; lina.segura@correounivalle.edu.co (L.M.S.-G.); john.ordonez@correounivalle.edu.co (J.E.O.); gustavo.zambrano@correounivalle.edu.co (G.Z.)

⁴ Center of Excellence on Novel Materials (CENM), Universidad del Valle, Edificio E20 No. 1026, Cali 760032, Colombia

⁵ Quantum Technologies, Information and Complexity Group, Departamento de Física, Universidad del Valle, Cali 760032, Colombia

* Correspondence: luz.gonzalez@unibague.edu.co

Abstract: We design and evaluate the performance of a one-dimensional photonic crystal (PhC) optical filter that comprises the integration of alternating layers of a barium titanate ferroelectric (BaTiO_3) and an yttrium oxide dielectric (Y_2O_3), with a critical high-temperature superconductor defect, yttrium–barium–copper oxide ($\text{YBa}_2\text{Cu}_3\text{O}_{7-x}$), resulting in the $(\text{BTO}/\text{Y}_2\text{O}_3)_N/\text{YBCO}/(\text{Y}_2\text{O}_3/\text{BTO})_N$ multilayered nanostructure array. Here, we demonstrate that such a nanosystem allows for routing and switching optical signals at well-defined wavelengths, either in the visible or the near-infrared spectral regions—the latter as required in optical telecommunication channels. By tailoring the superconductor layer thickness, the multilayer period number N , the temperature and the direction of incident light, we provide a computational test-bed for the implementation of a PhC-optical filter that works for both wavelength-division multiplexing in the 300–800 nm region and for high- Q filtering in the 1300–1800 nm range. In particular, we show that the filter’s quality factor of resonances Q increases with the number of multilayers—it shows an exponential scaling with N (e.g., in the telecom C-band, $Q \approx 470$ for $N = 8$). In the telecom region, the light transmission slightly shifts towards longer wavelengths with increasing temperature; this occurs at an average rate of 0.25 nm/K in the range from 20 to 80 K, for $N = 5$ at normal incidence. This rate can be enhanced, and the filter can thus be used for temperature sensing in the NIR range. Moreover, the filter works at cryogenic temperature environments (e.g., in outer space conditions) and can be integrated into either photonic and optoelectronic circuits or in devices for the transmission of information.

Keywords: photonic crystal filters; wavelength division multiplexing; optical communications; superconductors



Citation: González, L.E.; Segura-Gutierrez, L.M.; Ordoñez, J.E.; Zambrano, G.; Reina, J.H. A Multichannel Superconductor-Based Photonic Crystal Optical Filter Tunable in the Visible and Telecom Windows at Cryogenic Temperature. *Photonics* **2022**, *9*, 485. <https://doi.org/10.3390/photonics9070485>

Received: 8 June 2022

Accepted: 8 July 2022

Published: 12 July 2022

Publisher’s Note: MDPI stays neutral with regard to jurisdictional claims in published maps and institutional affiliations.



Copyright: © 2022 by the authors. Licensee MDPI, Basel, Switzerland. This article is an open access article distributed under the terms and conditions of the Creative Commons Attribution (CC BY) license (<https://creativecommons.org/licenses/by/4.0/>).

1. Introduction

Photonic crystals are periodic artificial structures of one, two or three dimensions. These configurations are characterized by optical parameters that change periodically (e.g., dielectric constants), thus allowing for the propagation of electromagnetic waves in media with a periodic spatial variation that can be tuned according to material composition and design, thus being particularly useful for the control of photon propagation and emission [1,2]. Such photonic crystal periodicity gives rise to a photonic band structure due to the scattered light from each interface between them materials composing the periodic

medium [3]; this, in turn, results in a coherent superposition of photons of specific energies, thus allowing for propagating and non-propagating electromagnetic modes, from which the latter is known as the photonic bandgap [3].

Due to these features, it is possible to control and tune light in PhCs [4], thus opening a new perspective for information processing and technological applications such as chips [5,6], filters [7,8], lasers [9,10], waveguides [11], integrated photonic circuits, sensors [12,13] and thin film photovoltaic cells [14,15], to mention but a few. As is well known, there exist many sort of materials used to form tunable PhCs, such as semiconductors [16], metals [17], superconductors [18,19], metamaterials [20] and liquid crystals [21], among others. In this work, we focus on a critical high-temperature superconductor material, $\text{YBa}_2\text{Cu}_3\text{O}_{7-x}$, as a defect layer inside the photonic crystal. Superconductor materials used for PhC fabrication present the following advantages: (i) the damping emission (losses) of electromagnetic waves that occur in metals are improved with the use of superconductors, and (ii) the superconductor dielectric function depends on the London penetration depth, which is a function of temperature and the external magnetic field. Due to this, high-temperature superconductor materials convey an interesting opportunity for the implementation of tunable photonic crystals in a wide variety of applications such as temperature sensors [17,22], polychromatic filters [23] and biosensors [24], among others.

Several technical reasons support the integration of high temperature superconductors (YBCO), ferroelectric (BTO) and dielectric ceramic materials (Y_2O_3) in a 1D photonic heterostructure. A key aspect is that all of them have a perovskite structure, good lattice matching and a chemical similarity [25–27], which allows the epitaxial growth to be successful; in addition, these materials bear thermal expansion and contraction owing to variations between ambient and cryogenic temperature [28]. Lastly, such a nanosystem is compatible with thin film filter technologies used in the optical fiber and optoelectronic device manufacturing industries [29].

In a previous work [19], we succeeded in experimentally realizing ferroelectric/superconductor 1D photonic crystals as suitable engineered nanosystems for tuning and controlling electromagnetic wave propagation in a wide region of the visible spectrum. We designed and experimentally demonstrated the optical reliability of the fabricated nanosystem via reflectance spectrometry measurements in the whole visible range and also theoretically modeled the optical response below and above the superconductor critical temperature. As a conclusion of our findings, and based on the implemented PhC, we proposed possible novel optical filters and reflectors which could transmit at high frequencies and operate at cryogenic temperatures [19].

To keep up with the global optical data traffic demands, the current generation of optical communication systems needs to increase its transmission capacity [30]. Wireless communication uses as its main transmission media the radio frequency (RF) spectrum. However, Infrared (IR) and Visible Light Communication (VLC) systems have become an alternative to RF due to their operation at high frequency regions with larger transmission bandwidth and an increment in the information-carrying capacity of the communication system [31,32]. In this context, an important issue is the need to develop novel devices that allow full control of light propagation throughout the visible and near-infrared (NIR) regimes, while minimizing losses during this process [33–37].

Here, we design and computationally characterize a novel optical filter built from a one-dimensional (1D) PhC that can be integrated into optical networks based on wavelength-division multiplexing (WDM), with a high- Q factor in the telecom region. These filters route and switch optical signals at a given wavelength in the visible or NIR ranges, following the spectral grids for WDM applications as per the ITU-T G.694.2 recommendation from the International Telecommunication Union (ITU) [38]. The photonic heterostructures are built from the integration of ferroelectric and ceramic materials and superconductors, and we report on their performance above and below the superconductor critical temperature. We show that such a nanosystem can allow the implementation of optical filters based on PhCs that are amenable for integration into photonic and/or optoelectronic circuits, or in devices

for the transmission of information in the visible and NIR ranges, at very low temperature environments (as in outer space conditions, to cite just one example).

2. Theoretical Framework

Figure 1 presents the geometry of the $(\text{BTO}/\text{Y}_2\text{O}_3)_N/\text{YBCO}/(\text{Y}_2\text{O}_3/\text{BTO})_N$ 1D tunable photonic filter. A defect superconductor layer ($\text{YBa}_2\text{Cu}_3\text{O}_{7-x}$) is sandwiched in a periodic multilayer stack composed of alternating layers of ferroelectric (BaTiO_3) and dielectric (Y_2O_3) materials, whose widths are d_s, d_a and d_b , respectively.

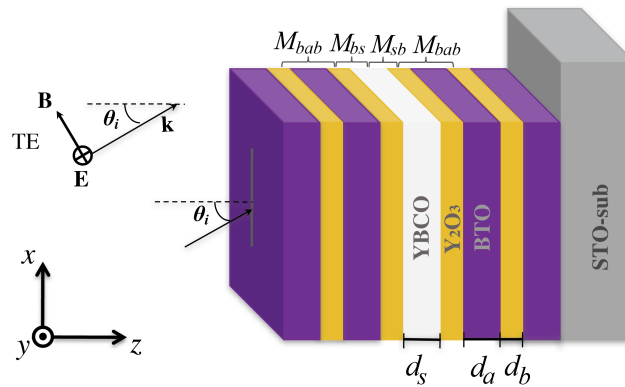


Figure 1. Schematics of the $(\text{BTO}/\text{Y}_2\text{O}_3)_N/\text{YBCO}/(\text{Y}_2\text{O}_3/\text{BTO})_N$ 1D tunable photonic filter, composed of alternating layers of BaTiO_3 and Y_2O_3 , with a $\text{YBa}_2\text{Cu}_3\text{O}_{7-x}$ superconductor defect layer, with corresponding widths d_a, d_b and d_s , respectively. One period, $N = 1$, $(\text{BTO}/\text{Y}_2\text{O}_3)_1/\text{YBCO}/(\text{Y}_2\text{O}_3/\text{BTO})_1$ corresponds to one bilayer of BaTiO_3 and Y_2O_3 saving a mirror symmetry respect to the YBCO superconductor defect layer. Thus, N periods refer to the number of repetitions of BaTiO_3 and Y_2O_3 bilayers. \mathbf{k} is the incident wave vector that fixes the direction of $\mathbf{E} \times \mathbf{B}$, and \mathbf{E} and \mathbf{B} denote the electric and magnetic fields, respectively. The light propagation is defined by θ_i , the angle with the z -axis, and xz is the plane of light incidence. M_{bab}, M_{bs} and M_{sb} indicate the transfer matrices in the intermediate layers ($\text{Y}_2\text{O}_3, \text{BaTiO}_3$ or $\text{YBa}_2\text{Cu}_3\text{O}_{7-x}$).

The propagation of an in-plane linearly polarized electromagnetic field of angular frequency ω is of the form $\vec{E}(z, t) = E(z)e^{-i\omega t}\hat{x}$ along the z -axis. By using Maxwell's equations for linear and isotropic media, the electric field amplitude $E(z)$ satisfies the equation [39–42]

$$\frac{d}{dz} \left[\frac{1}{n(z)Z(z)} \frac{dE(z)}{dz} \right] = -\frac{n(z)}{Z(z)} \frac{\omega^2}{c^2} E(z), \tag{1}$$

where c is the vacuum speed of light, $n(z) = \sqrt{\epsilon(z)}\sqrt{\mu(z)}$ and $Z(z) = \sqrt{\mu(z)}/\sqrt{\epsilon(z)}$ are the refraction index and impedance for each material layer, respectively.

A photonic crystal composed of alternating layers of different materials can be modeled by means of a function $\psi(z)$ by considering both the electric field and its first derivative to be continuous across their interface, which means that the function has two-components, as follows:

$$\psi(z) = \begin{pmatrix} E_z \\ \frac{1}{nZ} \frac{dE}{dz} \end{pmatrix}. \tag{2}$$

Equation (2) guarantees the continuity of the electric field and its derivative when it passes from one layer to another. This condition may be conveniently written by means of a characteristic transfer matrix M as

$$\psi(z) = M_i(z - z_0)\psi(z_0), \tag{3}$$

where z_0 denotes an arbitrary point in each material layer, and subscript i indicates the layer indexes; thus,

$$M_i = \begin{pmatrix} \cos\left(\frac{\omega|n_i|z}{c}\right) & \frac{|n_i|}{n_i} \frac{cZ_i}{\omega} \sin\left(\frac{\omega|n_i|z}{c}\right) \\ -\frac{|n_i|}{n_i} \frac{\omega}{cZ_i} \sin\left(\frac{\omega|n_i|z}{c}\right) & \cos\left(\frac{\omega|n_i|z}{c}\right) \end{pmatrix}. \tag{4}$$

By defining the transfer matrix from the superconductor defect layer to the Y_2O_3 layer of a first bilayer as M_{sb} (see Figure 1), the bilayer transfer matrix connecting $Y_2O_3/BTO/Y_2O_3$ layers as M_{bab} , and the transfer matrix connecting the Y_2O_3 layer with the superconductor defect layer as M_{bs} , the total transfer matrix for the entire $(BTO/Y_2O_3)_N/YBCO/(Y_2O_3/BTO)_N$ structure becomes

$$M_T = (M_{bab})^N M_{bs} M_{sb} (M_{bab})^N = \begin{pmatrix} P & \pm O \\ \pm R & S \end{pmatrix}. \tag{5}$$

where P, O, R and S correspond to the elements of the transfer matrix for $N = 1$. Since the matrix M_T is the transfer matrix of the whole system, its matrix elements determine the transmission and the reflection amplitudes for the entire system [40]. This enables us to determine the transmission amplitude of the entire system in terms of elements of the transfer matrices of the system’s constituents, so that the transmission through a single barrier can be written as

$$T_N = \left| \frac{1}{1 + M_{12}} \right|^2, \tag{6}$$

where M_{12} is the respective element of the transfer matrix for N periods. Finally, it is possible to obtain the transmission for N identical barriers; from Chebyshev’s identity, the N th power of the transfer matrix can be expressed as [40]

$$M_N = \begin{pmatrix} P U_{N-1} - U_{N-2} & O U_{N-1} \\ R U_{N-1} & S U_{N-1} - U_{N-2} \end{pmatrix}. \tag{7}$$

where $U_N = U_N(q) = \frac{\sin((N+1)qd)}{\sin qd}$ are the second-order Chebyshev polynomials. All numerical results for the transmission spectra were calculated by using the transfer matrix technique and performed in Wolfram Mathematica.

The Gorter–Casimir two-fluid model is adopted here to describe the electromagnetic response of the superconductor at non-zero temperature. Here, we consider that the superconductor material is non-magnetic ($\mu_2 = 1$) and that the relative permittivity of a lossless superconductor is given by [43] $\epsilon_2 = 1 - (\omega_{th}^2/\omega^2)$, where ω_{th} is the threshold frequency of the bulk superconductor, $\omega_{th}^2 = c^2/\lambda_L^2$, and λ_L is the temperature dependent penetration depth $\lambda_L^2 = \lambda_0^2 / [1 - (T/T_c)^p]$, where λ_0 is the so-called London penetration depth at $T = 0$ K, T_c is the superconductor critical temperature and $p = 2$ for a high temperature superconductor [43]. The threshold frequency exhibits a similar behavior to that of the plasma frequency in a Drude model for metals; that is, when the frequency $\omega > \omega_{th}$, ϵ_2 is positive and the electromagnetic (EM) waves can propagate in the superconductor. In contrast, the opposite behavior occurs for $\omega < \omega_{th}$, where the EM wave propagation is prohibited within the superconductor, and hence it constitutes an evanescent wave.

3. Results and Discussion

In order to produce the optical filter presented here, the strategy is to design and model a waveguide with a core of a low refractive index surrounded by a periodic multilayer reflector. We start with the design of an efficient periodic reflector such as a quarter-wave stack [44] built up of a number of quarter-wave layers of Y_2O_3 and $BaTiO_3$ materials. In particular, the quarter-wave reflector has been designed, although not restricted to this, for a normal angle of light incidence, that is, $\theta_i = 0$, and for a given operating wavelength in

the infrared and visible regions, centered at 1550 nm and 600 nm, respectively. To complete the optical filter, an ultrathin superconducting film was surrounded on each side by a periodic reflector containing N bilayers of BaTiO₃ and Y₂O₃.

Figure 2 plots the filter optical response for $N = 2$ in the wavelength region from 1300 nm to 1800 nm as a function of the whole range of incident angles for TE polarization at $T = 80$ K and $d_s = 10$ nm. In Figure 2a, the dark areas correspond to the high-reflectance ranges, while yellow areas indicate high transmission ranges where radiation passes through the structure. An interesting feature that arises is related to the light transmission through the structure: it has quite a sensitive response to the light incidence angle, as can be observed in the continuous displacement of the band to shorter wavelengths as the incident angle increases. In fact, one transmission band arises in the near-infrared region at 1600 nm at 0°, which continuously decreases to 1418 nm near 90°. We mention the importance of such a band since it lies within several spectral bands used in optical fiber communications (i.e., the E , S , C and L bands) [45].

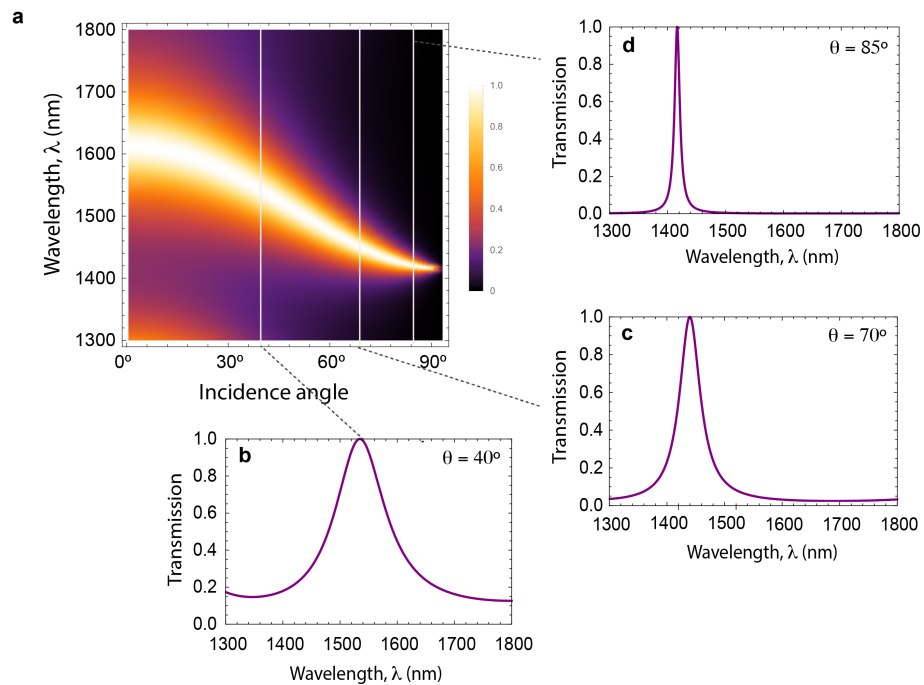


Figure 2. (a) Photonic crystal optical filter response for TE polarization in the whole range of incident angles at $T = 80$ K in the NIR range. The dark areas correspond to the high-reflectance ranges, and yellow regions indicate high transmission bands. White vertical lines in the figure are a guide to the eye, and correspond to the results for 40°, 70° and 85°, respectively. Panels (b–d) display the calculated transmittance of a (BTO/Y₂O₃)₂/YBCO/(Y₂O₃/BTO)₂ nanostructure, at $T = 80$ K and incidence angles of 40°, 70° and 85°, for TE polarization, respectively.

The incidence angle θ_i denotes the angle with the z -axis defined in the range of $0^\circ \sim \pm 90^\circ$, xz is the plane of light incidence, and the direction of $\mathbf{E} \times \mathbf{B}$ is given by the incident wave vector \mathbf{k} , where \mathbf{E} and \mathbf{B} represent the electric and magnetic fields, respectively (see Figure 1). To compute the transmittance spectra, we first consider a BaTiO₃ layer thickness $d_a = 160$ nm, and $d_a = 62$ nm for estimations in the infrared and visible regions, respectively. Here, we consider an operation temperature that varies from 20 K to 80 K; hence, the BaTiO₃-dielectric function can be considered constant, $\epsilon = 5.8$ [46–48]. In turn, the Y₂O₃ layer thickness $d_b = 201$ nm, and $d_b = 78$ nm, for the corresponding calculations in the infrared and visible regions, respectively; the Y₂O₃ dielectric constant $\epsilon = 3.76$ [49]. The considered superconductor defect layer YBa₂Cu₃O₇ exhibits $p = 2$, $T_c = 92$ K, $\lambda_0 = 145$ nm at $T = 0$ K, and a dielectric function ϵ_2 , as described above.

In Figure 2b–d, we plot the transmittance behavior for spectra computed at incident angles of 40° , 70° and 85° , respectively. The sharp peaks in these figures mean that the $(\text{BTO}/\text{Y}_2\text{O}_3)_2/\text{YBCO}/(\text{Y}_2\text{O}_3/\text{BTO})_2$ nanostructure can indeed be configured as a narrow-band filter [44]. These results show noticeable changes in the transmission band width with the incident angle, which narrows as the angle of incidence approaches 90° . In such a way, for angles closer to 90° , the shape of the transmission peak changes, allowing for a bandpass filter over a narrower range. Then, if the light incidence angle is varied by a small amount, it is possible to tune the bandpass over a narrow range of wavelengths. For example, Figure 2d shows that the optical nanostructure allows the passage of light at only a narrow set of wavelengths around 1430 nm. This transmission peak is abruptly attenuated for the other wavelength ranges, resulting in a transmission coefficient that goes to zero. This result is in agreement with the fact that when a wave impinges at a right angle, it moves parallel to the separation surface of the two media, and therefore its energy is not transmitted through the surface [50].

Although the quarter-wave reflector has been designed for a particular operating wavelength of 1550 nm and for a normal angle of incidence, it remains efficient even when used at other wavelengths and incidence angles, as can be seen in Figure 2. This is due to the refractive index contrast, which plays a key role in the reflector efficiency when used outside of its design regime [50]. According to this, in order to implement the optical filter and to transmit a signal at 1550 nm, e.g., for $N = 2$ (see Figure 2), we use the bandgap of the multilayer reflector to be able to spatially localize the electromagnetic mode at the defect superconducting layer. We remark that the choice of operating wavelength for the IR optical filter at 1550 nm (and normal incidence) is based on the extremely low loss of the standard single-mode fiber for telecommunications wavelengths at such wavelength (1550 nm; C-band) [51]; this is a key feature to bear in mind in the design and construction of the proposed optical filters.

We point out that a localized mode in the defect layer can exist even though it is well known that no EM modes are allowed to have frequencies in the gap. This is so because, when light of a given frequency is sent into a photonic band gap (PBG), the wave vector becomes complex and the wave amplitude decays exponentially into the crystal, originating evanescent modes, which in turn decay exponentially. This is why we include a defect layer in the construction of the filter: by breaking the PhC translation symmetry, we are able to sustain an evanescent mode and to excite a localized mode with frequencies inside the PBG [44]. This localized mode associated with the defect—henceforth, the defect state or resonance—corresponds to the single transmission peak that is reported in Figures 2 and 3.

We next analyze a key feature that characterizes the $(\text{BTO}/\text{Y}_2\text{O}_3)_N/\text{YBCO}/(\text{Y}_2\text{O}_3/\text{BTO})_N$ 1D filter performance. In Figure 3, we plot the optical response of the designed filter in terms of the period number N , in the wavelength range from 1300 nm to 1800 nm, for a TE polarization, $d_s = 30$ nm, at $T = 80$ K. Figure 3a–c displays the light transmission/reflection through the proposed tunable photonic filter for $N = 2, 5$ and 8, respectively. As in the previous figure, we obtain a monotonic displacement of the transmission band towards shorter wavelengths as the incident angle increases. The resonant peak becomes thinner with increasing N , which indicates the sensitivity of the quality of the filtered signal with the number of periods N used in the filter's construction.

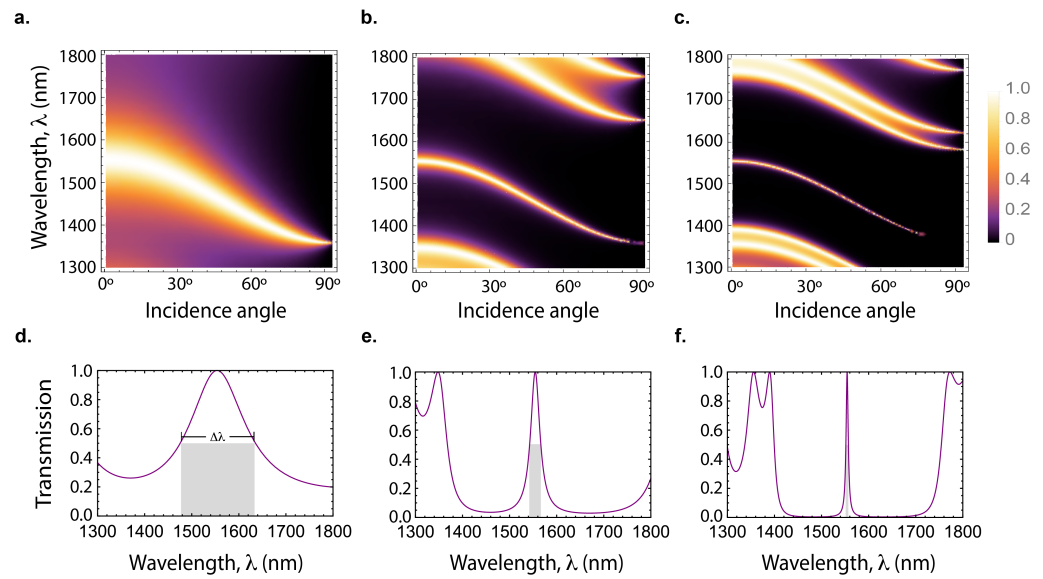


Figure 3. Optical filter response in the whole range of incident angles, for period numbers (a) $N = 2$, (b) $N = 5$, and (c) $N = 8$; $T = 80$ K and $d_s = 30$ nm. The resonant peak becomes thinner with increasing N and angle of incidence, which act as key parameters in the quantification of the filtered signal quality. Panels (d–f) present the transmission spectra of the 1D tunable resonant filter $(\text{BTO}/\text{Y}_2\text{O}_3)_N/\text{YBCO}/(\text{Y}_2\text{O}_3/\text{BTO})_N$ at normal incidence, as a function of the wavelength and the filter’s period number. The graphs show a 100% peak at defect resonance wavelength $\lambda_c = 1550$ nm for (d) $N = 2$, $Q \sim 10$, (e) $N = 5$, $Q \sim 66$, and (f) $N = 8$, $Q \sim 470$. The gray shaded regions indicate the FWHM transmission characterized by $\Delta\lambda$. The quality factor $Q \equiv \lambda_c/\Delta\lambda$ scales exponentially with N .

To quantify the sensitivity of the resonant peak with N , in Figure 3d–f, we consider the transmission spectra at normal incidence for $T = 80$ K, $d_s = 30$ nm and $N = 2, 5$ and 8 , respectively. $\Delta\lambda$ corresponds to the full width at half maximum (FWHM), and λ_c indicates the operating wavelength of the filter. In each case, the defect supports a resonant mode with a wavelength at 1550 nm. However, what is markedly different is the peak width. We quantify such a transmission peak width (or resonance) by means of the quality factor, Q [44,52]. The value $1/Q$ is a dimensionless quantity interpreted as the fractional bandwidth of the resonance, which is related to the outgoing power and the electromagnetic energy localized in the defect. This key parameter for measuring the performance of a filter briefly means that the larger Q , the higher the quality of the optical filter.

The fractional width $\Delta\lambda/\lambda_c$ at half-maximum (50% transmission) is identically equal to $1/Q$, a factor commonly used to certify a filter as narrowband or broadband. The gray shaded regions in Figure 3d–f indicate the transmission peak width at half-maximum, $\Delta\lambda$, whose approximate values are 159.6 nm, 23.6 nm and 3.3 nm, respectively. Thus, the corresponding quality factors can be estimated as $Q \approx 10$ for $N = 2$, $Q \approx 66$ for $N = 5$, and $Q \approx 470$ for $N = 8$, which means that Q exhibits an exponential scaling with the number of periods N . These Q values can be interpreted in several ways: as a dimensionless decay rate, as a dimensionless lifetime or as a fractional bandwidth of the resonance [44]. In any case, a notable feature is that Q can be tailored by changing the number of periods in the structure; hence, it is a key parameter that enables the performance optimization of the designed optical filter.

Figure 4 displays the effect of temperature on the optical response for the $(\text{BTO}/\text{Y}_2\text{O}_3)_5/\text{YBCO}/(\text{Y}_2\text{O}_3/\text{BTO})_5$ optical ($N = 5$) filter at normal incidence, in the wavelength range from 1300 nm to 1800 nm, for a TE polarization with $d_s = 30$ nm. As in the previous case, dark areas correspond to the high reflectance ranges, while yellow areas indicate transmission ranges where radiation passes through the PhC filter. To gain further insight into

the temperature effect on the optical response, in Figure 4b, we present the amplification image of Figure 4a in the wavelength range from 1520 nm to 1570 nm. As shown, the transmission peak can be tuned about 15 nm over the filter operating range by changing the temperature from 20 K to 80 K. Furthermore, in Figure 4c, we plot a better visualization of this feature. The results for 30 K, 50 K and 70 K, corresponding to purple, red and orange curves, respectively, evidence the small shift in the transmission peak by about 5 nm each 20 K, approximately. We associate this finding primarily with the slight decrease suffered by the superconductor dielectric constant as the wavelength increases, a result that is in agreement with the electromagnetic variational principle [44]. This effect may also be accounted for by considering the layers' slight thermal expansion or contraction produced by the temperature variation.

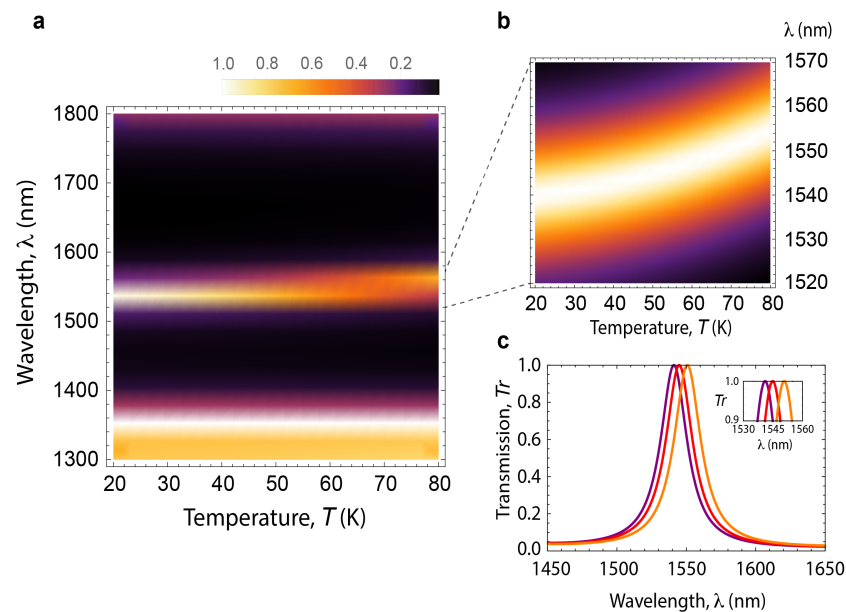


Figure 4. (a) Simulated photonic band structure of the $(\text{BTO}/\text{Y}_2\text{O}_3)_5/\text{YBCO}/(\text{Y}_2\text{O}_3/\text{BTO})_5$ filter ($N = 5$) as a function of wavelength and temperature T , in the region $T = 20$ K to 80 K, with $d_s = 30$ nm, at normal incidence. The dark areas correspond to the high-reflectance ranges, and yellow regions indicate high transmission bands where radiation passes through the structure. (b) Optical response amplification of the $N = 5$ PhC filter to a wavelength range between 1520 nm and 1570 nm. (c) Transmission light behavior of the $N = 5$ filter as a function of temperature for $T = 30$ K (purple line), $T = 50$ K (red line) and $T = 70$ K (orange line), respectively.

We next examine the details of the band dependence on the superconductor defect layer thickness, d_s . In Figure 5a, we plot the optical response of the $N = 5$ PhC filter in the superconductor thickness range from 1 to 90 nm. It is known that a transmission filter can be achieved by adding a structural defect that can be any geometrical or material perturbation of a system that continuously preserves the translational symmetry in the multilayer plane [50]. In our case, this is a single layer of YBCO at the center of a 1D photonic crystal according to $(\text{BTO}/\text{Y}_2\text{O}_3)_5/\text{YBCO}/(\text{Y}_2\text{O}_3/\text{BTO})_5$. This implementation ensures that the defect mode is located inside a bandgap of a surrounding photonic crystal, resulting in an exponentially fast decay of a modal field outside the defect layer.

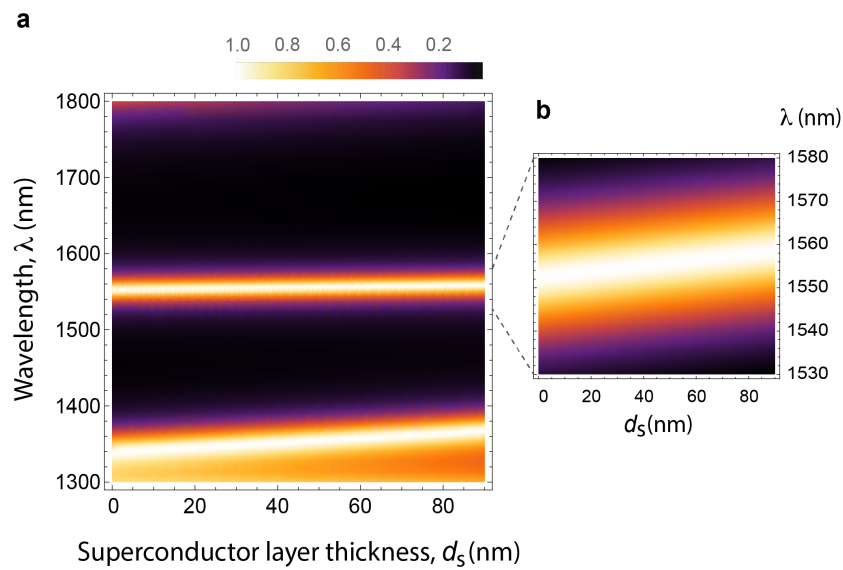


Figure 5. (a) Simulated photonic band structure of the $(\text{BTO}/\text{Y}_2\text{O}_3)_5/\text{YBCO}/(\text{Y}_2\text{O}_3/\text{BTO})_5$ filter as a function of wavelength and superconductor layer thickness for $T = 80$ K at normal incidence. (b) Filter optical response amplification in the range 1530 nm–1580 nm.

Figure 5a makes it evident that such a defect mode corresponds to the transmission peak at 1550 nm, concentrating its electromagnetic energy in the vicinity of the YBCO defect layer. On the other hand, in Figure 5b, we plot a zoom of Figure 5a in the wavelength range from 1530 nm to 1580 nm. It turns out that the transmission peak can be tuned in about 10 nm over the filter operating range by varying the superconductor defect layer thickness from 1 nm to 90 nm. This behavior leads us to conclude that the optical response does not considerably change with the variation of the YBCO defect layer thickness in this telecom band. The designed IR optical filter has a guiding mechanism that is based on the low refractive index of the superconducting defect layer; hence, this does not rely on its thickness. Note that our result comprises an effective refractive index of the superconducting defect layer guided mode, n_s , which is smaller than the BTO and Y_2O_3 refractive indices. This arrangement corresponds to the so-called lower-refractive-index core photonic-bandgap waveguides [50]. As explained above, our filter’s core is built with a superconducting defect layer (size d_s and low refractive index), surrounded by a quarter-wave reflector with refractive indices $n_{\text{Y}_2\text{O}_3} = 1.93$ [49] and $n_{\text{BTO}} = 2.43$ [46]; hence, $n_s < n_{\text{Y}_2\text{O}_3} < n_{\text{BTO}}$, which opens a possibility for efficient light guidance in the low-refractive-index superconductor defect layer.

We now analyze the filter optical response in the visible region. In Figure 6, we compute for the $N = 2$ filter in the wavelength range from 300 nm to 800 nm as a function of the whole range of incident angles for TE polarization at $T = 80$ K, and $d_s = 10$ nm. A similar behavior was obtained in comparison with the IR optical case, that is, light transmission through the structure has a sensitive response to the light incidence angle, and this can be observed in the continuous displacement of the band to shorter wavelengths as the incident angle increases. In addition, with the incidence angle variation from 45° to 85° , a transition from pseudo to full optical gap is obtained.

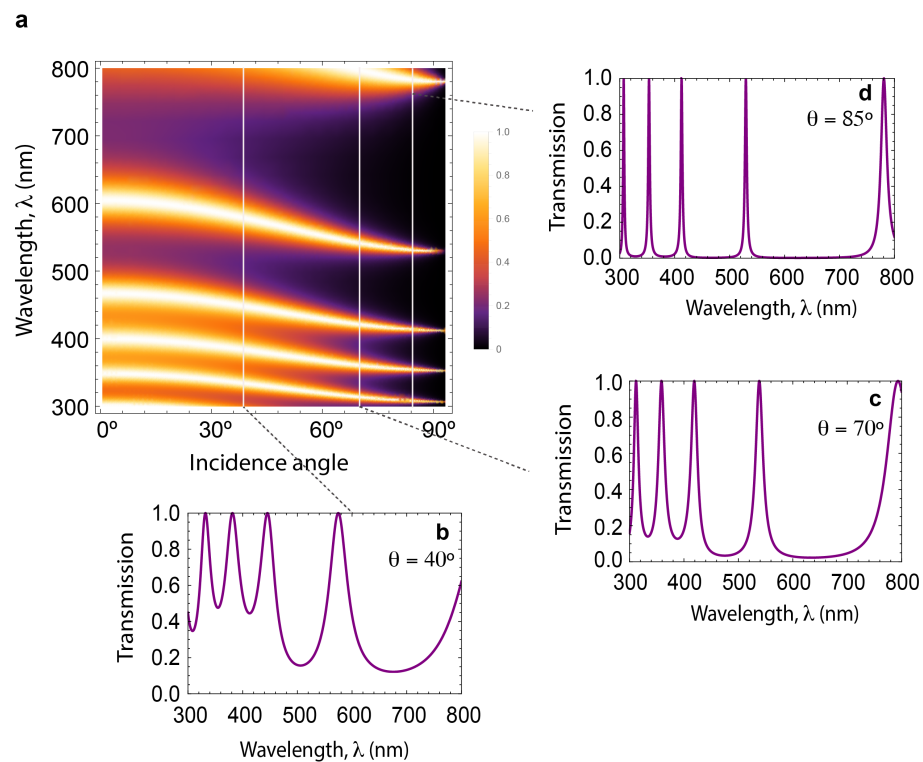


Figure 6. (a) Optical response of the $(\text{BTO}/\text{Y}_2\text{O}_3)_2/\text{YBCO}/(\text{Y}_2\text{O}_3/\text{BTO})_2$ filter in the visible spectral region, for TE polarization in the whole range of incident angles at $T = 80$ K. The dark areas correspond to the high-reflectance ranges, and yellow regions indicate high transmission bands where radiation passes through the structure. Panels (b–d) display the measured transmittance at incident angles of 40° , 70° and 85° (marked by the white vertical lines in (a)), respectively.

The defect mode or resonant peak in the visible spectra range is located inside a bandgap at 600 nm. We remark that this transmission peak is surrounded by other peaks that become of a very narrow wavelength width as the angle of incidence approaches 90° , which means a higher Q -factor. This fact can be used in the design of a multichannel transmission filter for WDM implementation, and hence the use of more than one transmission peak in a single configuration can be engineered. As VLC uses the visible range of the electromagnetic spectrum from 380 to 780 nm as the carrier, an order of magnitude faster than current radio frequency (RF) systems, optical devices operating within this spectral range represent an advantage over RF ones. We notice that the visible spectrum is unregulated and does not require a license to operate. In addition, VLC systems achieve a higher data transmission rate by increasing the number of channels by means of WDM technology [31,32]. Based on this result, we put forward a strategy for WDM in visible light communication: the presented $(\text{BTO}/\text{Y}_2\text{O}_3)_2/\text{YBCO}/(\text{Y}_2\text{O}_3/\text{BTO})_2$ PhC optical filter enables the use of multiple light wavelength channels to send and transmit data. As can be clearly seen in Figure 6, several signals could be transmitted via the optical filter at different wavelengths or frequencies on the optical spectrum. Moreover, the number of wavelength channels for the WDM implementation can be enlarged by increasing the number N of multilayers in the nanostructure.

In summary, we have presented and evaluated the performance of a ferroelectric–dielectric–superconductor filter built from one-dimensional photonic crystals, where the superconductor acts as a defect layer. The assessment of the performance has been given in terms of physical variables that involve the direction of the incident radiation, the number of multilayers, temperature and the width of the superconductor defect layer. Thus, we have validated two important properties of the 1D resonant tunneling filter: its operating wavelength and its resonant mode lifetime. The operating wavelength can be controlled by the geometry and symmetry of the structure, i.e., by the $\text{Y}_2\text{O}_3/\text{BTO}$ quarter-wave stacks

on both sides of the superconducting defect: these behave like wavelength-specific mirrors that localize the light within a finite region. The resonant mode lifetime, characterized by the quality factor Q , can be tailored by changing the number of periods of the quarter-wave stack. These results can be used for integration into optical networks that are based on wavelength division multiplexing.

4. Conclusions

We have engineered and computationally tested the performance of a $(\text{BTO}/\text{Y}_2\text{O}_3)_N/\text{YBCO}/(\text{Y}_2\text{O}_3/\text{BTO})_N$ 1D photonic crystal optical filter whose optical response provides a platform to route and switch optical signals at tailored wavelengths that can be exploited for data transmission and telecommunication purposes either in the visible spectrum or the NIR spectral region, especially at the commercially available optical telecom bands.

In the visible spectral region, the filter can be used for multichannel transmission in WDM applications, whereby five possible transmission bands have been identified (for the case $N = 2$). Moreover, the number of bands can be tailored by engineering the structural filter parameters (N and thickness of material layers), temperature and incident light conditions.

In the NIR region, we have obtained a one-channel transmission filter within the spectral band used in optical fiber communications (1260–1675 nm). A key result from an operational point of view is that, at normal incidence, temperature may tune the frequency range of the transmission peak at an average rate of 0.25 nm/K in the range from 20 K to 80 K, which indicates that the filter can be used for temperature sensing in the NIR range.

We have demonstrated that the larger the number of multilayers N , the higher the quality factor Q . In fact, we found that Q scales with N in an exponential manner. In particular, in the telecom band, we achieved a high $Q \approx 470$ for $N = 8$ (at 80 K and normal incidence). Finally, we expect that our findings will open a way for the development of novel photonic crystal materials that can be integrated into photonic and superconducting circuitry and optoelectronics, or in other sorts of devices that require the transmission of information in the visible and IR range environments.

Author Contributions: L.E.G., J.E.O., L.M.S.-G., G.Z. and J.H.R. contributed to the analysis and writing of the manuscript and to the discussion, corrections, feedback and comments. L.E.G. performed the analytical and numerical calculations. All authors have read and agreed to the published version of the manuscript.

Funding: This work has been supported by Vicerrectoría de Investigaciones at Universidad del Valle (Grant CI 71267). L.E.G. is grateful to Universidad de Ibagué for financial support (CI 21-002-ESP).

Institutional Review Board Statement: Not applicable.

Informed Consent Statement: Not applicable.

Data Availability Statement: Not applicable.

Conflicts of Interest: The authors declare no conflict of interest.

References

1. Yablonovitch, E. Photonic crystals. *J. Mod. Opt.* **1994**, *41*, 173–194. [[CrossRef](#)]
2. Vinet, L.; Zhedanov, A. *Photonic Crystals: Physics and Technology*; Springer: Milan, Italy, 2008.
3. McGurn, A. *Nanophotonics*; Springer International Publishing: Berlin/Heidelberg, Germany, 2018.
4. Yoshino, K.; Shimoda, Y.; Kawagishi, Y.; Nakayama, K.; Ozaki, M. Temperature tuning of the stop band in transmission spectra of liquid-crystal infiltrated synthetic opal as tunable photonic crystal. *Appl. Phys. Lett.* **1999**, *75*, 932. [[CrossRef](#)]
5. Li, H.; Low, M.X.; Ako, R.T.; Bhaskaran, M.; Sriram, S.; Withayachumnankul, W.; Kuhlmeier, B.T.; Atakaramians, S. Broadband Single-Mode Hybrid Photonic Crystal Waveguides for Terahertz Integration on a Chip. *Adv. Mater. Technol.* **2020**, *5*, 2000117. [[CrossRef](#)]
6. Clementi, M.; Iadanza, S.; Schulz, S.A.; Urbinati, G.; Gerace, D.; O’Faloain, L.; Galli, M. Thermo-Optically Induced Transparency on a photonic chip. *Light Sci. Appl.* **2021**, *10*, 240. [[CrossRef](#)]
7. Mbakop, F.K.; Tom, A.; Dadjé, A.; Vidal, A.K.C.; Djongyang, N. One-dimensional comparison of $\text{TiO}_2/\text{SiO}_2$ and Si/SiO_2 photonic crystals filters for thermophotovoltaic applications in visible and infrared. *Chin. J. Phys.* **2020**, *67*, 124. [[CrossRef](#)]

8. Soltani, O.; Zaghdoudi, J.; Kanzari, M. Tunable filter properties in 1D linear graded magnetized cold plasma photonic crystals based on Octonacci quasi-periodic structure. *Photonics Nanostruct.-Fundam. Appl* **2020**, *38*, 100744. [[CrossRef](#)]
9. Sakata, R.; Ishizaki, K.; De Zoysa, M.; Fukuhara, S.; Inoue, T.; Tanaka, Y.; Iwata, K.; Hatsuda, R.; Yoshida, M.; Gellela, J.; et al. Dually modulated photonic crystals enabling high-power high-beam-quality two-dimensional beam scanning lasers. *Nat. Commun.* **2020**, *11*, 3487. [[CrossRef](#)]
10. Butler, S.M.; Singaravelu, P.K.J.; O'Faolain, L.; Hegarty, S.P. Long cavity photonic crystal laser in FDML operation using an akinetic reflective filter. *Opt. Express* **2020**, *28*, 38813. [[CrossRef](#)]
11. Shi, C.; Yuan, J.; Luo, X.; Shi, S.; Lu, S.; Yuan, P.; Xu, W.; Chen, Z.; Yu, H. Transmission characteristics of multi-structure bandgap for lithium niobate integrated photonic crystal and waveguide. *Opt. Commun.* **2020**, *461*, 125222. [[CrossRef](#)]
12. Baghbadorani, H.K.; Barvestani, J. Sensing improvement of 1D photonic crystal sensors by hybridization of defect and Bloch surface modes. *Appl. Surf. Sci.* **2021**, *537*, 147730. [[CrossRef](#)]
13. Mehaney, A.; Abadla, M.M.; Elsayed, H.A. 1D porous silicon photonic crystals comprising Tamm/Fano resonance as high performing optical sensors. *J. Mol. Liq.* **2021**, *322*, 114978. [[CrossRef](#)]
14. Delgado-Sanchez, J.M.; Lillo-Bravo, I. Angular dependence of photonic crystal coupled to photovoltaic solar cell. *Appl. Sci.* **2020**, *10*, 1574. [[CrossRef](#)]
15. Zheng, W.; Luo, X.; Zhang, Y.; Ye, C.; Qin, A.; Cao, Y.; Hou, L. Efficient Low-Cost All-Flexible Microcavity Semitransparent Polymer Solar Cells Enabled by Polymer Flexible One-Dimensional Photonic Crystals. *ACS Appl. Mater. Interfaces* **2020**, *12*, 23190. [[CrossRef](#)] [[PubMed](#)]
16. Aly, A.H.; Ghany, S.E.A.; Kamal, B.M.; Vigneswaran, D. Theoretical studies of hybrid multifunctional ($\text{YBa}_2\text{Cu}_3\text{O}_{7-x}$) photonic crystals within visible and infra-red regions. *Ceram. Int.* **2020**, *46*, 365. [[CrossRef](#)]
17. Zaky, Z.A.; Aly, A.H. Theoretical Study of a Tunable Low-Temperature Photonic Crystal Sensor Using Dielectric-Superconductor Nanocomposite Layers. *J. Supercond. Nov. Magn.* **2020**, *33*, 2983. [[CrossRef](#)]
18. González, L.E.; Ordoñez, J.E.; Zambrano, G.; Porras-Montenegro, N. $\text{YBa}_2\text{Cu}_3\text{O}_7/\text{BaTiO}_3$ 1D Superconducting Photonic Crystal with Tunable Broadband Response in the Visible Range. *J. Supercond. Nov. Magn.* **2018**, *31*, 2003. [[CrossRef](#)]
19. González, L.E.; Ordoñez, J.E.; Carlos, A.; Melo, L.; Mendoza, E.; Reyes, D.; Zambrano, G.; Porras-Montenegro, N.; Granada, J.C.; Gómez, M.E.; et al. Experimental realisation of tunable ferroelectric/superconductor $(\text{BTO}/\text{YBCO})_N/\text{STO}$ 1D photonic crystals in the whole visible spectrum. *Sci. Rep.* **2020**, *10*, 13083. [[CrossRef](#)]
20. Segal, N.; Keren-Zur, S.; Hendlar, N.; Ellenbogen, T. Controlling light with metamaterial-based nonlinear photonic crystals. *Nat. Photonics* **2015**, *9*, 180. [[CrossRef](#)]
21. Schlafmann, K.R.; White, T.J. Retention and Deformation of the Blue Phases in Liquid Crystalline Elastomers. *Nat. Commun.* **2021**, *12*, 4916. [[CrossRef](#)]
22. Chen, H.; Chen, Z.; Yang, H.; Wen, L.; Yi, Z.; Zhou, Z.; Dai, B.; Zhang, J.; Wu, X.; Wu, P. Mult-mode Surface plasmon resonance absorber base don dat-type single-layer graphene. *RSC Adv.* **2022**, *12*, 7821. [[CrossRef](#)]
23. Soltani, O.; Francoeur, S.; Baraket, Z.; Kanzari, M. Tunable polychromatic filters based on semiconductor-superconductor-dielectric periodic and quasi-periodic hybrid photonic crystal. *Opt. Mater.* **2020**, *111*, 110690. [[CrossRef](#)]
24. Hao, J.; Gu, K.; Xia, L.; Liu, Y.; Yang, Z.; Yang, H. Research on low-temperature blood tissues detection biosensor based on one-dimensional superconducting photonic crystal. *Commun. Nonlinear Sci. Numer. Simulat.* **2020**, *89*, 105299. [[CrossRef](#)]
25. Ravanamma, R.; Reddy, K.M.; Krishnaiah, K.V.; Ravi, N. Structure and morphology of yttrium doped barium titanate ceramics for multi-layer capacitor applications. *Mater. Today Proc.* **2021**, *46*, 259. [[CrossRef](#)]
26. Yang, Q.; Deng, J.; Wang, G.; Deng, Q.; Zhao, J.; Dai, Y.; Duan, P.; Cui, M.; Kong, L.; Gao, H.; et al. The physical properties and microstructure of $\text{BiFeO}_3/\text{YBCO}$ heterostructures. *Vacuum* **2019**, *167*, 313–318. [[CrossRef](#)]
27. Chacón, M.; Bolaños, G.; Lopera, W.; Prieto, P. Tunneling Characteristics of Epitaxial $\text{YBa}_2\text{Cu}_3\text{O}_{7-x}/\text{Y}_2\text{O}_3/\text{YBa}_2\text{Cu}_3\text{O}_{7-x}$ Planar Type Junctions. *Phys. Supercond.* **1997**, *287*, 711. [[CrossRef](#)]
28. Li, L. Ferroelectric/superconductor heterostructure. *Mater. Sci. Eng. R Rep.* **2000**, *29*, 153. [[CrossRef](#)]
29. Macleod, H.A. *Thin-Film Optical Filters*; Taylor & Francis: Boca Ratón, FL, USA, 2018.
30. Won, R. Is it crunch time? *Nat. Photonics* **2015**, *9*, 424. [[CrossRef](#)]
31. Lian, J.; Vatanserver, Z.; Noshad, M.; Brandt-Pearce, M. Indoor visible light communications, networking, and applications. *J. Phys. Photonics* **2019**, *1*, 012001. [[CrossRef](#)]
32. Haas, H.; Elmighani, J.; White, I. Optical Wireless Communication. *Philos. Trans. R. Soc. A* **2020**, *378*, 20200051. [[CrossRef](#)]
33. Eriksson, T.A.; Hirano, T.; Puttnam, B.J.; Rademacher, G.; Luís, R.S.; Fujiwara, M.; Namiki, R.; Awaji, Y.; Takeoka, M.; Wada, N.; Sasaki, M. Wavelength division multiplexing of continuous variable quantum key distribution and 18.3 Tbit/s data channels. *Commun. Phys.* **2019**, *2*, 9. [[CrossRef](#)]
34. Feng, C.; Ying, Z.; Zhao, Z.; Gu, J.; Pan, D.Z.; Chen, R.T. Wavelength division multiplexing (WDM) based integrated electronic-photonic switching network (EPSN) for high-speed data processing and transportation. *Nanophotonics* **2020**, *9*, 4579. [[CrossRef](#)]
35. Chhipa, M.K.; Radhouene, M.; Robinson, S.; Suthar, B. Improved dropping efficiency in two-dimensional photonic crystal-based channel drop filter for coarse wavelength division multiplexing application. *Opt. Eng.* **2017**, *56*, 015107. [[CrossRef](#)]
36. Sabne, A.; Panda, A.; More, V. Simplified Wavelength Division Multiplexing in Visible Light Communication by Using RGB LED as Frequency Selective Receiver. In Proceedings of the 10th International Conference on Computing, Communication and Networking Technologies (ICCCNT), Kanpur, India, 6–8 July 2019; p. 45670.

37. Zhang, H.; Lu, Y.; Duan, L.; Zhao, Z.; Shi, W.; Yao, J. Intracavity absorption multiplexed sensor network based on dense wavelength division multiplexing filter. *Opt. Express* **2014**, *22*, 24546. [[CrossRef](#)] [[PubMed](#)]
38. Minoli, D. *Telecommunications Technology Handbook*; Artech House: London, UK, 2003.
39. Cavalcanti, S.B.; de Dios-Leyva, M.; Reyes-Gómez, E.; Oliveira, L.E. Photonic band structure and symmetry properties of electromagnetic modes in photonic crystals. *Phys. Rev. E* **2007**, *75*, 026607. [[CrossRef](#)]
40. Markos, P.; Soukoulis, C. *Wave Propagation: From Electrons to Photonic Crystals and Left-Handed Materials*; Princeton University Press: Princeton, NJ, USA, 2008.
41. Deng, Y.; Cao, G.; Yang, H.; Zhou, X.; Wu, Y. Dynamic control of double plasmon-induced transparencies in aperture-coupled waveguide-cavity system. *Plasmonics* **2018**, *13*, 345. [[CrossRef](#)]
42. Zheng, Z.; Luo, Y.; Yang, H.; Yi, Z.; Zhang, J.; Song, Q.; Yang, W.; Liu, C.; Wu, X.; Wu, P. Thermal tuning of terahertz metamaterial absorber properties based on VO₂. *Phys. Chem. Chem. Phys.* **2022**, *24*, 8846. [[CrossRef](#)]
43. Orlando, T.; Delin, K. *Foundations of Applied Superconductivity*; Electrical Engineering Series; Addison-Wesley: Boston, MA, USA, 1991.
44. Joannopoulos, J.D.; Johnson, S.G.; Winn, J.N.; Meade, R.D. *Photonic Crystals: Molding the Flow of Light*; Princeton University Press: Princeton, NJ, USA, 2009.
45. Karothu, D.P.; Dushaq, G.; Ahmed, E.; Catalano, L.; Polavaram, S.; Ferreira, R.; Li, L.; Mohamed, S.; Rasras, M.; Naumov, P. Mechanically robust amino acid crystals as fiber-optic transducers and wide bandpass filters for optical communication in the near-infrared. *Nat. Commun.* **2021**, *12*, 1326. [[CrossRef](#)]
46. Wemple, S.; Didomenico, M.; Camlibel, I. Dielectric and optical properties of melt-grown BaTiO₃. *J. Phys. Chem. Solids* **1968**, *29*, 1797. [[CrossRef](#)]
47. Kay, H.F.; Vousden, P. Symmetry changes in barium titanate at low temperatures and their relation to its ferroelectric properties. *Philos. Mag. J. Sci.* **1949**, *40*, 1019. [[CrossRef](#)]
48. Merz, W.J. The Electric and Optical Behavior of BaTiO₃ Single-Domain Crystals. *Phys. Rev.* **1949**, *76*, 1221. [[CrossRef](#)]
49. Nigara, Y. Measurement of the optical constants of Yttrium Oxide. *Jpn. J. Appl. Phys.* **1968**, *7*, 404. [[CrossRef](#)]
50. Skorobogatiy, M.; Yang, J. *Fundamentals of Photonic Crystal Guiding*; Cambridge University Press: Cambridge, UK, 2009.
51. Zhang, J.; Wu, R.; Wang, M.; Fang, Z.; Lin, J.; Zhou, J.; Gao, R.; Chu, W.; Cheng, Y. High-index-contrast single-mode optical waveguides fabricated on lithium niobate by photolithography assisted chemo-mechanical etching. *Jpn. J. Appl. Phys.* **2020**, *59*, 086503. [[CrossRef](#)]
52. Deng, Y.; Cao, G.; Wu, Y.; Zhou, X.; Liao, W. Theoretical description of dynamic transmission characteristics in MDM waveguide aperture-side-coupled with ring cavity. *Plasmonics* **2015**, *10*, 1537. [[CrossRef](#)]